Article

Interface Kinetics Assisted Barrier Removal in Large Area 2D-WS$_2$ Growth to Facilitate Mass Scale Device Production

Abid [1], Poonam Sehrawat [1], Christian M. Julien [2,*] and Saikh S. Islam [1,*]

1 Centre for Nanoscience and Nanotechnology, Jamia Millia Islamia (A Central University), New Delhi 110025, India; abid.zak@gmail.com (A.); sehrawatpoonam@gmail.com (P.S.)

2 Institut de Minéralogie, de Physique des Matériaux et de Cosmologie (IMPMC), Sorbonne Université, CNRS-UMR 7590, 4 Place Jussieu, 75252 Paris, France

* Correspondence: christian.julien@sorbonne-universite.fr (C.M.J.); sislam@jmi.ac.in (S.S.I.)

Abstract: Growth of monolayer WS$_2$ of domain size beyond few microns is a challenge even today; and it is still restricted to traditional exfoliation techniques, with no control over the dimension. Here, we present the synthesis of mono- to few layer WS$_2$ film of centimeter^2 size on graphene-oxide (GO) coated Si/SiO$_2$ substrate using the chemical vapor deposition CVD technique. Although the individual size of WS$_2$ crystallites is found smaller, the joining of grain boundaries due to sp^2-bonded carbon nanostructures (~3–6 nm) in GO to reduced graphene-oxide (RGO) transformed film, facilitates the expansion of domain size in continuous fashion resulting in full coverage of the substrate. Another factor, equally important for expanding the domain boundary, is surface roughness of RGO film. This is confirmed by conducting WS$_2$ growth on Si wafer marked with few scratches on polished surface. Interestingly, WS$_2$ growth was observed in and around the rough surface irrespective of whether polished or unpolished. More the roughness is, better the yield in crystalline WS$_2$ flakes. Raman mapping ascertains the uniform mono-to-few layer growth over the entire substrate, and it is reaffirmed by photoluminescence, AFM and HRTEM. This study may open up a new approach for growth of large area WS$_2$ film for device application. We have also demonstrated the potential of the developed film for photodetector application, where the cycling response of the detector is highly repetitive with negligible drift.

Keywords: chemical; vapor deposition; graphene oxide; transition-metal dichalcogenides; WS$_2$

1. Introduction

Lamellar two-dimensional (2D) WS$_2$ has immense potential for electronic applications because of its remarkable properties such as tunable direct bandgap [1–3], high photoluminescence intensity [4,5], high emission quantum field [6], attractive spin-orbit coupling [6], substantial exciton/trion binding energies [7–9], etc., which give WS$_2$ superior leverage over other transition-metal dichalcogenides (TMDCs). Unfortunately, the research on WS$_2$ is not matured yet, especially large-scale production of single-crystal monolayers [10–12]. Challenges lie in reliable synthesis of atomically thick 2D layers and controlled manipulation of electronic properties [13]. Though mechanical cleaving still remains a relatively facile technique to prepare high quality single to few layered WS$_2$, problems such as absence of control over thickness, relatively small lateral size and low yield limit its applications and commercialization [14,15]. The most popular techniques to produce few-layered WS$_2$ include intercalation driven exfoliation [16], liquid phase exfoliation [17], physical vapor deposition [18], hydrothermal reaction [19], and heat treatment of W and S containing precursors [20]. However, the domain size of developed WS$_2$ via aforementioned methods is generally restricted to a few microns (μm), and the production of WS$_2$ monolayer films with desired domain size remains a distant dream. To achieve this, several strategies (e.g., atomic layer deposition [21], pulsed-laser deposition [22,23], metal/metal oxide thin films [24], suitable metal substrates [25], etc.), have been suggested

to achieve uniform dispersion of precursors over substrates. Presently, large scale continuous growth of TMDCs is highly complex and expensive, and results in poor quality films [9].

Chemical vapor deposition (CVD) remains a challenge for a long time for growing two-dimensional TMDC materials with high crystallinity, desired thickness, and sufficient domain size [10,12,26–28]. For WS_2 growth, typical synthesis approach involves sulfidation of WO_3 powders at sufficiently high temperature. The growth conditions such as precursor type, process step, and their manipulations during growth, are found to greatly affect the product quality. Most of the reports on CVD grown WS_2 solely bank on vapor phase reaction between S and W precursors at suitably high temperatures, where a single furnace is used for both precursors. In such systems, there is no control over the temperature of individual precursor, thereby limiting the parameter space of growth reaction [28]; leading to poor uniformity and repeatability. High melting point of WO_3 powders and sulfurization rate are found to influence the growth process. Achieving large triangle shaped growth is challenging, because of lower vapor pressure of WO_3 due to its high melting temperature (1473 °C) [29]. This is a serious problem and severely lowers the partial pressure of WO_3 vapors [29]. Further, the low vapor pressure of WO_3 also hampers the availability of W atoms on substrate surface. Thus, enhancing the partial pressure of WO_3 vapors is a natural approach to obtain large sized WS_2 flakes [12]. This can be accomplished by reducing the pressure of the furnace. However, this increases the S vapor transfer speed, thereby increasing the sulfurization rate [10]. Fast sulfurization is not desirable for the transport and diffusion of precursor vapors on a substrate and may result in aggregation of precursors at certain locations on the substrate, thereby limiting the growth of large sized WS_2 crystals [10,30,31]. An efficient way involves a trade-off between the increase in partial pressure of WO_3 vapors and lower the transfer speed of S vapors.

Recently, many researchers have focused on developing monolayer WS_2 via CVD. Zhang et al. employed low-pressure chemical vapor deposition (LPCVD) technique to synthesize atomically thin triangle shaped WS_2 crystals on sapphire substrate having single domain size ~50 μm [32]. An improvement was introduced in the CVD process by Cong et al. to effectively increase the concentration of precursors and furnace pressure [33]. They achieved single-domain growths of ~178 μm [33]. Li et al. introduced further changes in the CVD reaction by employing alkali metal halides as growth promoters [34]. The groups of Zhang [32] and Li [34] reported that due to strong reducing nature, the mixing of suitable amount of H_2 enhances the sublimation and sulfurization of WO_3 precursor. Fu et al. [35] investigated the influence of CVD reaction temperature and gas flow rate (comprising a mixture of 97% Ar and 3% H_2) on the growth size and morphology of WS_2 films. The optimized growth conditions yielded a domain size of ~52 μm. Rong's group [28] achieved precise control over S introduction time by utilizing a two-zone furnace and obtained very large area WS_2 films of 370 μm domain size. Recently, Liu et al. [36] reported sequential synthesis of several one-, and two-dimensional nanomaterials by intentionally creating initial low sulfur conditions, to divide the growth process in two stages: the first stage is a partial reduction and the second one is sulfurization. By this, they could exploit a WO_{3-x} intermediate route, and were able to grow large size WS_2 (150 μm).

TMDCs growth is very susceptible to substrate treatment prior to formation [37]. To assist the nucleation by seeding the substrate with various aromatic molecules, such as -3,4,9,10-tetracarboxylic acid tetrapotassium salt (PTAS), perylene-3,4,9,10-tetracarboxylic dianhydride (PTCDA), and reduced graphene oxide (RGO), perylene encourages the lateral growth of TMDCs. However, this seeding technique helps to grow the large area mono-to few layer TMDCs but continuous film from the abovementioned technique is still limited. Although the CVD method has many advantages, the coordination among various growth parameters is highly complex and requires further elucidation.

In this work, we present a novel approach for large area synthesis of WS_2 on graphene oxide (GO) surface via CVD under high temperature conditions of 1070 °C. Upon transformation to RGO during growth process, GO becomes a mixed sp^3-sp^2 bonded network,

where nano-sized sp^2-patches of size ~3–6 nm, are randomly distributed with more than 60–70% coverage [38–40]. The sp^2-patches are six-fold aromatic carbon atoms with C=C bonds, whereas major percentage of sp^3 bonds constitutes epoxides (C–O) and hydroxyl (−OH) groups in the basal plane and somewhat lesser amount of carboxyl (−COOH) and carbonyl (−C=O) functionalities in the edges [38–40]. These sp^2-chemical bonds act as a seed to promote the growth of large area WS_2 film. The as-developed WS_2 layers are polycrystalline comprising mainly mono- to few layers. The single-crystal domains are triangular and hexagonal in shape, with sizes up to 60 μm on Si/SiO_2 and ~15 μm on the GO coated Si/SiO_2, respectively. The domain size of WS_2 film on GO coated Si/SiO_2 is much smaller than that on non-GO substrate, but the development of large continuous surface makes a great footprint in WS_2 growth, attributed to C=C assisted coalescence of high-density polycrystalline grain boundaries into large domain area. Suitable explanation is given how sp^2-patches comprised of C=C bonds are pivotal in the expansion of domain size of WS_2 film. Surface roughness of the top layer of substrate is a well-recognized technique for nucleation of nanostructure growth and is cross-checked with intentionally created rough surface on silicon wafer. The proposed device fabrication technique is well suited for mass production of identical devices, and therefore bids for commercial scale development. Moreover, this technique can be extended to the fabrication of other TMDCs. We have further demonstrated the use of the developed film for photodetector applications.

2. Materials and Methods

WO_3 powders (≥99.995% trace metals basis), sulfur (≥99.998% trace metals basis), natural graphite powders (flakes size: 45 μm, ≥99.99% trace metals basis), and sodium nitrate ($NaNO_3$, ≥99.995% trace metals basis) were commercially secured from Sigma Aldrich, India. Sulfuric acid (H_2SO_4) and potassium permagnate ($KMnO_4$) have been supplied by Thermo Fisher Scientific, India and DI water was obtained from Merck (Darmstadt, Germany). For experimental purposes, only analytical grade materials/chemicals were procured and used as received.

The morphology, size and structure of as-synthesized WS_2 were examined via a transmission electron microscope (TEM) (JEOL JEM F-200, Tokyo, Japan) working at 200 kV. The samples for TEM investigations were kept on the conventional holey carbon Cu grid. High-resolution transmission electron microscopy (HRTEM, JEOL, Tokyo, Japan) studies reveal the uniformity and high quality of WS_2 samples grown on both Si/SiO_2 and GO coated Si/SiO_2 substrates. Basic studies of WS_2 growth and the domain size were performed on an optical microscope (Leica DM4 P, Wetzlar, Germany). Raman spectrophotometers (WITec Alpha 300RA, Ulm, Germany and LabRAM HR800 HORIBA JY, Kyoto, Japan) fitted with a Peltier cooled CCD detector and confocal microscope were operated for verifying the crystallinity, defects and number of layers. A diode laser of excitation wavelength 532 nm was used to excite the samples. A 100X objective lens with spot size of 1 μm was used to focus the excitation onto the samples. The thickness of grown sample was analyzed by atomic force microscopy (AFM) fitted with the Raman system. Surface morphology of the CVD grown WS_2 on Si/SiO_2 and GO coated Si/SiO_2 was studied on a scanning electron microscope (SEM) (Nova Nano SEM 450, FEI, Oregon, USA). The photoluminescence (PL) measurements were performed by fluorescence spectrometer (Agilent Technologies, Carry Eclipse fluorescence spectrometer, California, USA). For PL investigations, the prepared samples were dispersed in ethanol by simply ultrasonicating the growth substrate for few minutes and isolating the upper one-third solution into a quartz cuvette.

3. Results and Discussion

Two approaches have been adopted to synthesize monolayer WS_2 of large domain size, where CVD is employed to grow WS_2 on two substrates, i.e., Si/SiO_2 and GO-coated Si/SiO_2 ($Si/SiO_2/GO$), with the aim to extend the domain size of WS_2 and uniform coverage of the entire substrate area (see Sections 3.1 and 3.2).

3.1. First Approach: Mono- to Few-Layered WS$_2$ Growth on Si/SiO$_2$

WS$_2$ growth was carried out inside a two-zone tube furnace having separate high- and low-temperature zones, denoted as HT and LT, respectively, as shown in Figure 1a. Ultrahigh purity argon at flow rate of 100 sccm under atmospheric pressure was used as carrier gas to transport sulfur vapors to the HT zone. In a typical experiment, WO$_3$ powders (200 mg of pure grade 99.9%) was placed in an alumina crucible at the center of HT-zone of the furnace. Si/SiO$_2$ substrate (10 mm $\times$ 10 mm) was placed on the alumina crucible in inverted position so as to allow WO$_3$ vapor to hits the substrate and deposit on it. The sulfur powder (400 mg of pure grade 99.5%) was loaded upstream, and heated in LT-zone of the furnace. The HT- and LT-zone temperatures were controlled in such a way that the temperature in both the zones simultaneously reach at 1070 °C and 220 °C, respectively [28]. Monolayer WS$_2$ grains were grown on Si/SiO$_2$ substrate having small domain size and the growth remained scattered. The reaction occurring at the surface of the substrate can be summarized as:
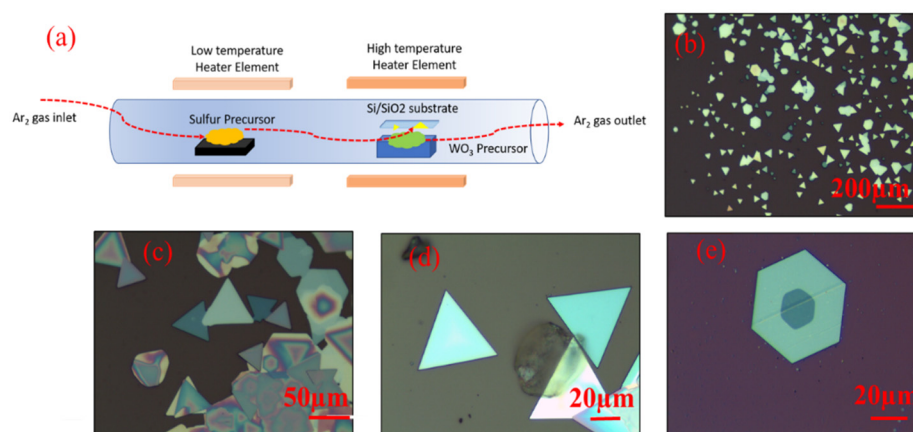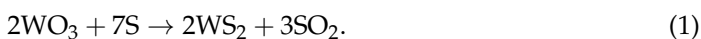
$$2WO_3 + 7S \rightarrow 2WS_2 + 3SO_2. \tag{1}$$

Figure 1. (**a**) Experimental setup. (**b**–**e**) Optical images of synthesized WS$_2$ film showing the presence of mono-to-few layered WS$_2$ on Si/SiO$_2$ substrate.

Thus, the vapor phase reaction between tungsten oxide and sulfur, produces tungsten disulfide and sulfur dioxide as end products. The optimized time duration for WS$_2$ growth is found to be 45 min, once the temperature of HT zone reaches 1070 °C. After completing the growth process, the CVD system was allowed to cool naturally to the room temperature.

Figure 1b–e shows the optical images of the WS$_2$ sample grown on Si/SiO$_2$ substrate. Two types of crystallites are visible: (a) equilateral triangles, and (b) hexagons; both are characteristic of WS$_2$ single crystal formation. Most of the crystals include monolayers. However, bi- and tri-layered regions are also visible at the center of large monolayer crystals, which is supposed to be the nucleation site, even for further growth of multi-layers [41].

Formation of hexagons in case of multilayer grains originates from the random orientation of individual WS$_2$ layers and differences in crystal orientation, where each orientation acts as nucleation site [41–43]. The side length of the crystals in case of equilateral triangles is found to be ~60 µm, which is reasonably large. The CVD growth of TMDCs is generally believed to be a self-limiting process [44]. The lateral size of WS$_2$ increases with the partial pressure of chalcogen precursors [45], while its thickness is determined by the partial pressure of transition metal precursors [46]. We have kept the weight of sulfur powders to be the twice of the weight WO$_3$ (chalcogen precursor). Thus, the lateral growth dominates in our case and could explain the growth of large size single crystals [46]. Furthermore, we could find WS$_2$ single crystals in variable sizes, ranging from 100 nm to 60 µm on the same Si/SiO$_2$ substrate. The growth duration is found to directly influence the area

of grown crystals, before the crystal growth reaches its limit. Therefore, large sized WS_2 crystals can be formed if the growth time is kept sufficiently long.

- Electron Microscope Analysis

Figure 2a–c shows the FESEM images of WS_2 samples deposited on Si/SiO$_2$ substrate, corroborating the findings of optical microscopy, indicating both equilateral triangles and hexagons. In case of WS_2, the growth of equilateral triangles suggests single crystallinity; whereas the hexagonal or star-like structures result from several rotationally symmetric grains [4,9,26,46,47]. The size distribution histogram of hexagonal and triangle flakes of WS_2 is shown in Figure 2d–e. Where the average size of the hexagonal and triangular flake is found to be 71.5 µm and 44.5 µm, respectively. The ratio of the hexagon to the triangular flakes over the substrate is 2:1. Notably, the growth products, though consisting of monolayers, are scattered over the substrate and do not cover the entire substrate surface.
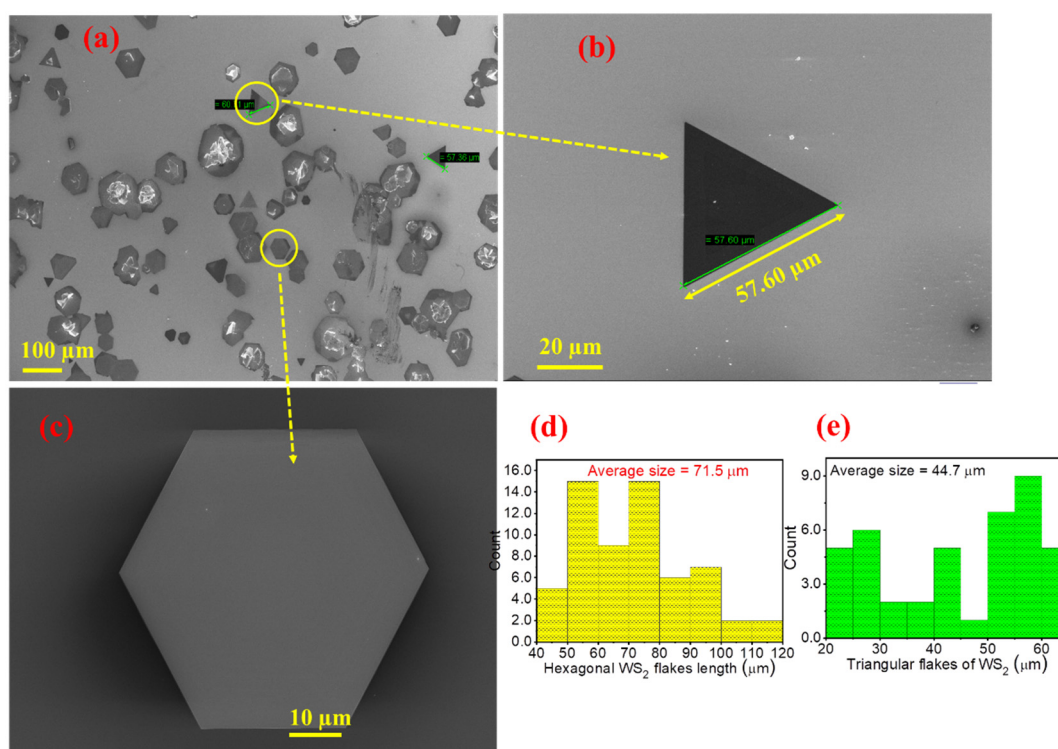

Figure 2. (**a**–**c**) FESEM micrographs of the WS_2 layers grown on Si/SiO$_2$ substrate at various magnification levels and (**d**,**e**) Size distribution histogram of hexagonal and triangle WS_2 flakes.

Figure 3a–c shows a low magnification bright field TEM imaging of WS_2 crystals suspended on a holey carbon Cu grid. For TEM imaging, first the WS_2 grown onto the Si/SiO$_2$ substrate was ultrasonicated in ethanol for 20 min to get the WS_2 flakes. After this, the suspension was centrifuged at a speed of 3000 rpm for 15 min to remove unwanted contamination or to allow settling down of heavy particles. Finally, top one-third supernatant was used for TEM analysis. We used HRTEM and selected area electron diffraction (SAED) to characterize the WS_2 domains. Figure 3a shows the hexagonal flakes with lateral dimension of about ~2.5 µm. In Figure 3b, the distorted cum truncated WS_2 triangle is clearly observable. At higher resolutions (Figure 3c,d), the crystalline nature of the flakes is clearly displayed. In Figure 3e, the selected area electron diffraction (SAED) pattern is indicated, which further confirms the highly crystalline morphology of as-grown WS_2.
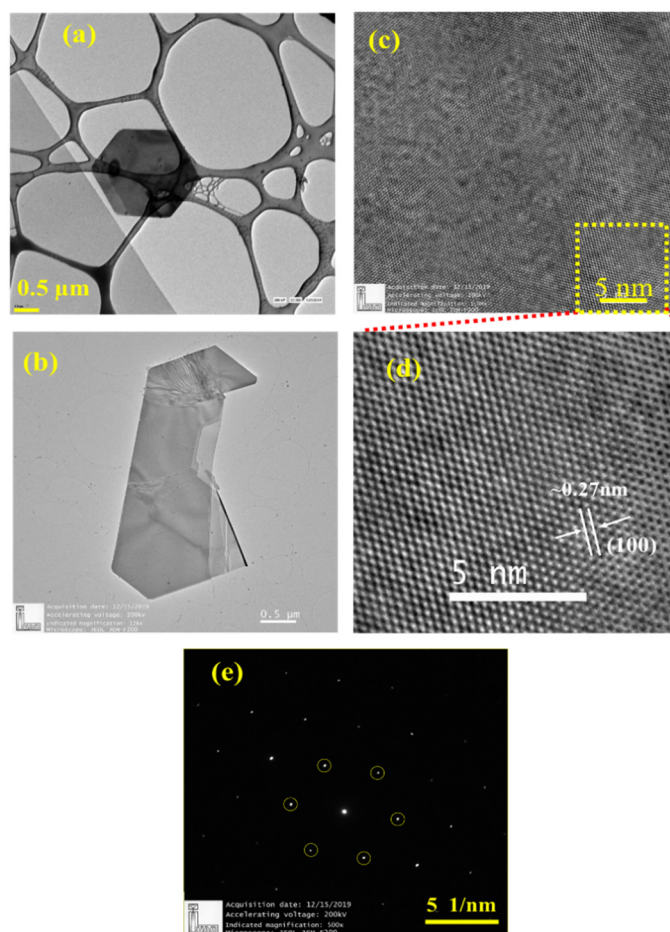
Figure 3. The TEM images of WS$_2$ flakes shown in (**a**,**b**) both at low magnification, (**c**) at high magnification. (**d**) zoomed view of (**c**), and (**e**) SAED pattern of the zoomed area.

- Raman Analysis

The *E-k* diagram and the phonon dispersion in Brillouin zone for WS$_2$ are shown in Figure 4a–c. Raman spectroscopy was employed to detect both the in-plane (E_{2g}^1) and out-of-plane (A_{1g}) phonon modes. Figure 4d shows Raman spectrum of the WS$_2$ flakes deposited over the Si/SiO$_2$ substrate, indicating a strong peak at 354 cm^{-1} (2LA(M)), signifying a longitudinal acoustic mode at M point. This signals the monolayer growth of WS$_2$ [9,26]. The peak at 421 cm^{-1} corresponding to the A_{1g} mode, although weak, is also observed. As is widely reported, the separation between these two peaks increases from 67 to 72 cm^{-1} with increasing the number of layers from single- to tri-layer due to a red-shifting of 2LA(M) mode [26,48–51]. However, the observed peak separation of ~67 cm^{-1} is the fingerprint of WS$_2$ monolayer growth. Its topography, revealing a triangular shape probed via Atomic Force Microscopy (AFM), is shown in Figure 4e,f. The whole crystal is almost atomically flat and clean. The height profile in Figure 4f indicates the as-grown WS$_2$ on Si/SiO$_2$ having a step size of 0.89 nm; reaffirming the growth of a WS$_2$ monolayer. To verify the uniformity in the flakes, Raman mapping studies were performed from one edge to the other (Figure 5a,b). The synthesized WS$_2$ flakes were further analyzed by recording multiple Raman spectra across the area of post WS$_2$ grown substrate. Typically, seven measurement sites were selected on the top surface, and it can be concluded that we have achieved the monolayered WS$_2$ flakes. As seen in Figure 5a,b, the spots 1 and 7 only show the Raman-active LO mode of Si, while spots 2, 3, 4, 5, and 6 express the Raman features of WS$_2$ monolayers, and interestingly, the Raman result is also found supplemented by AFM studies.
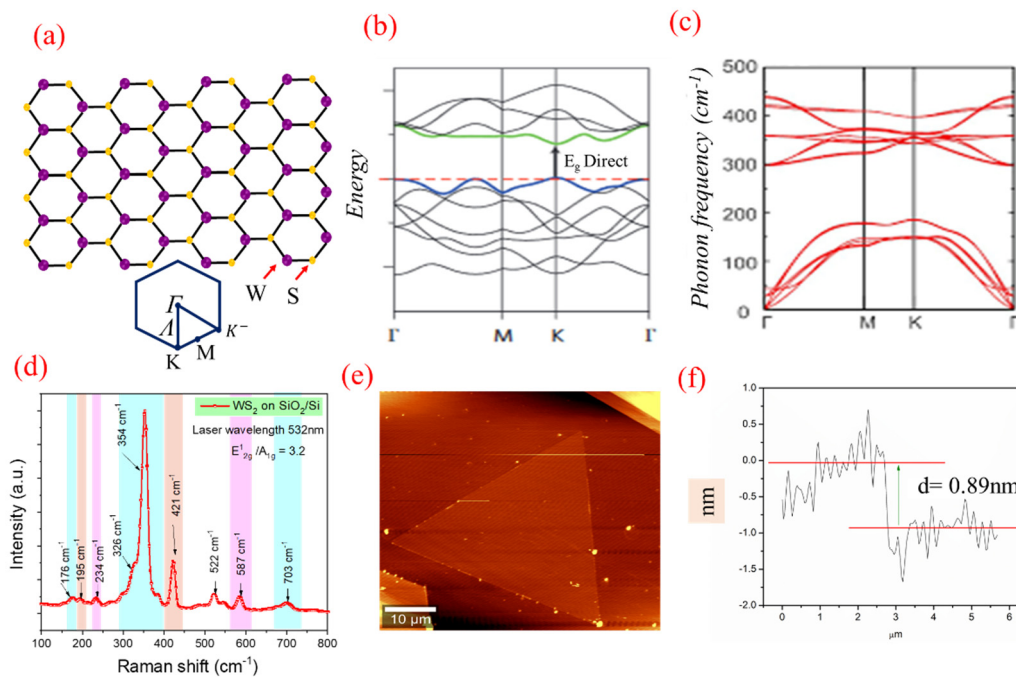
Figure 4. (**a**) Real space lattice structure and Brillouin zone in reciprocal space, (**b**) electronic band structure (*E-K* diagram), (**c**) phonon dispersion, (**d**) Raman spectrum, (**e**) AFM image of WS$_2$ monolayer crystal grown on Si/SiO$_2$ substrate and (**f**) AFM cross-section height profile for the deposited sample revealing a thickness of the grown film to be ~0.89 nm.
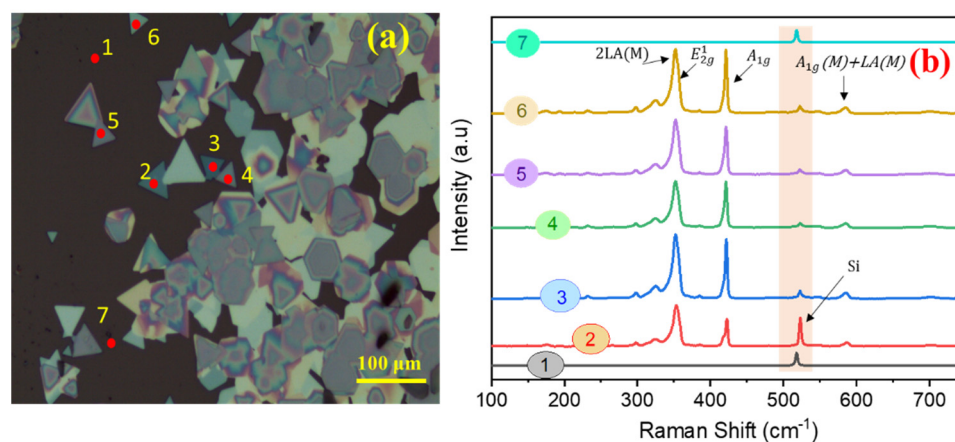

Figure 5. (**a**) Optical microscope image of WS$_2$ deposited over Si/SiO$_2$, indicating the selected measurement spots, and (**b**) Raman spectra of the spots identified in (**a**) where peak at 520 cm^{-1} in all the spectra is the LO mode of the silicon wafer.

- Photoluminescence (PL) Analysis

The PL properties of 2D-TMDCs are mainly governed by their excitonic features [1,7–9,52]. In the limiting case of 2D materials, as shown in Figure 6a, the lines of electric field between the hole and electron start extending beyond the material, thereby reducing the dielectric screening and enhancing coulomb interactions [36,38,39]. A strong coulombic force is the main reason behind strong photoemission efficiency. This enhanced coulomb interaction suggests formation of bound e-h pairs or "excitons", having greater binding energies making them stable even at room temperature [7,52–54]. In case of monolayer 2D material, significant deviation is expected from the hydrogenic model, prevalent to describe Wannier-excitons in inorganic semiconducting materials [7,51]. Therefore, the calculation of binding energy of excitons in case of single-layered WS$_2$ needs to consider modified potential [54]. High intense peak is observed at 630 nm (1.968 eV) in the as-synthesized

monolayer WS_2, which mainly originates from neutral-exciton (X_A) emission due to direct transition between the lowest conduction band (CB) and the highest valence band (VB) at the same *K*-point in the Brillouin zone [7,49,55–58], and schematically represented in Figure 4c. The fundamental bandgap of a single layer WS_2 is ~2.1 eV, but the large excitonic binding energy of 0.032 eV renders the optical bandgap measured at 1.968 eV [8,50–52] as shown schematically in Figure 6a,c shows the PL spectra of WS_2 flakes on the Si/SiO_2 substrate. Figure 6b represents the Neutral A-excitonic transition (XA) in the energy level diagram. The FWHM values of the PL spectra lie between 25 to 35 meV for both the approaches which is in accordance with the literature and further establish the fact of monolayer formation [59,60]. The presence of enhanced coulombic interaction at higher distant points suggests more likelihood of formation of higher-order excitons, i.e., trions and bi-excitons [51].
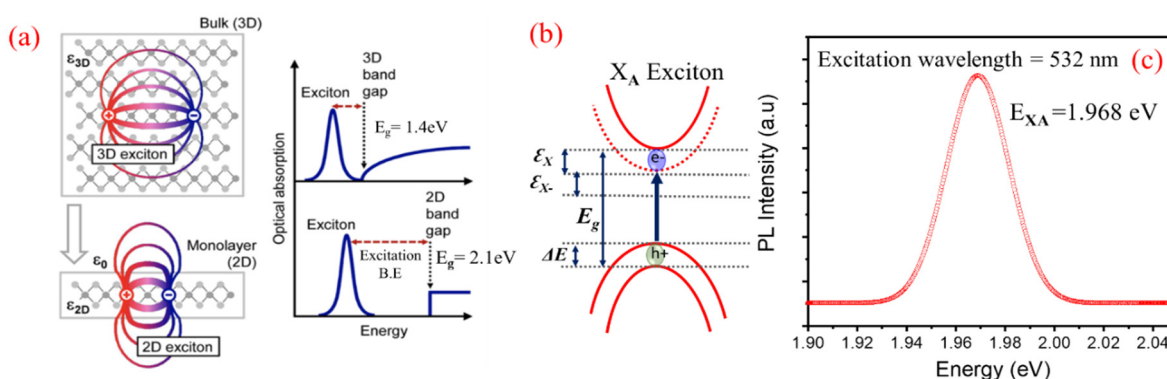

Figure 6. (**a**) Schematic diagram showing the reduced dielectric screening on the e-h pair bonding in a typical 2D material [38–40]. (**b**) Neutral A-excitonic transition (X_A) in the energy level diagram, and (**c**) PL spectra of WS_2 grown over Si/SiO_2 substrate.

3.2. Second Approach: Uniform Growth of WS_2 Flakes on Spin-Coated GO

In this approach, we have spin coated pre-synthesized graphene oxide (GO) solution over the Si/SiO_2 substrate prior to CVD growth. Hummers' method [38–40] has emerged as a well-established technique to prepare graphite oxide which can then be ultrasonicated to yield graphene oxide (GO). Briefly, natural graphite powders (5.0 g), H_2SO_4 (120 mL) and $NaNO_3$ (2.5 g) were mixed via continuous stirring. During stirring, the temperature was kept below 10 °C in order to check overheating of the mixture. After obtaining a uniform mixing, $KMnO_4$ (15.0 g) was added to this mixture by stirring for 24 h at room temperature. A condensed light brown colored slurry was obtained, which was diluted with deionized water (150 mL) and stirring for 2 h at 98 °C. The resulting mixture was vigorously washed with HCl and deionized water, to yield graphite oxide. Subsequently, graphite oxide was ultrasonicated (37 kHz, 500 W) for 3 h. The resulting suspension was centrifuged at 5000 rpm and GO was obtained by collecting the top one-third supernatant from the centrifugation product. A suspension of GO was prepared by mixing 5 mg GO in deionized water via ultrasonication. The substrate for WS_2 growth was prepared by spin coating (2500 rpm) 100 μL GO suspension on a Si/SiO_2 wafer. Figure 7a includes the SEM micrograph of the GO film coated over Si/SiO_2 substrate. The GO flakes appear uniformly dispersed over the surface of the substrate, and are expected to act as a seed layer for the growth of WS_2 film. In Figure 7b, the Raman spectrum of the GO film is displayed in 500–3500 cm^{-1} range, in which the D-, G- and 2D-band are clearly defined at 1354, 1592, and 2712 cm^{-1}, respectively. Further, XRD analysis was performed to confirm the quality of prepared GO. The XRD pattern in Figure 7c shows the peak at $2\theta \approx 11°$, which validates the high quality of the GO flakes.
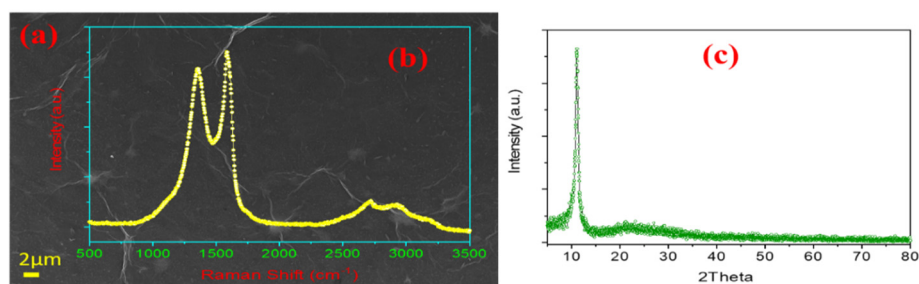
Figure 7. (**a**) FESEM micrograph, (**b**) Raman spectrum, and (**c**) XRD pattern of the GO film deposited on Si/SiO$_2$ substrate before the growth of the WS$_2$ layer.

The WS$_2$ growth was performed similar to that described in Section 3.1 (i.e., WS$_2$ grown at Si/SiO$_2$ substrate). The only difference is the coating of Si/SiO$_2$ substrate with GO, which is expected to get converted into RGO due to in-situ heating encountered in the HT-zone during the growth process. The synthesis process is schematically illustrated in Figure 8a–c. Figure 8d–g shows the Optical images of the WS$_2$ grown on the GO coated Si/SiO$_2$, where in Figure 8d clear interface is shown between WS$_2$ film and the Si substrate. Figure 8h–k shows the FESEM micrographs at different magnification. In this approach, sufficient amount of sulfur vapor is taken into consideration for the reaction, similar to the first approach. Here, it is noteworthy to say that the sp^2-carbon nanostructures in the RGO matrix fulfill three-pronged objectives: (i) they improve the surface adhesion, thereby enhancing local adsorption of WO$_3$ molecules; (ii) they reduce WO$_3$ to yield WO$_{3-x}$; and finally, (iii) they also act as active sites for heterogeneous nucleation, as demonstrated in Figure 9.
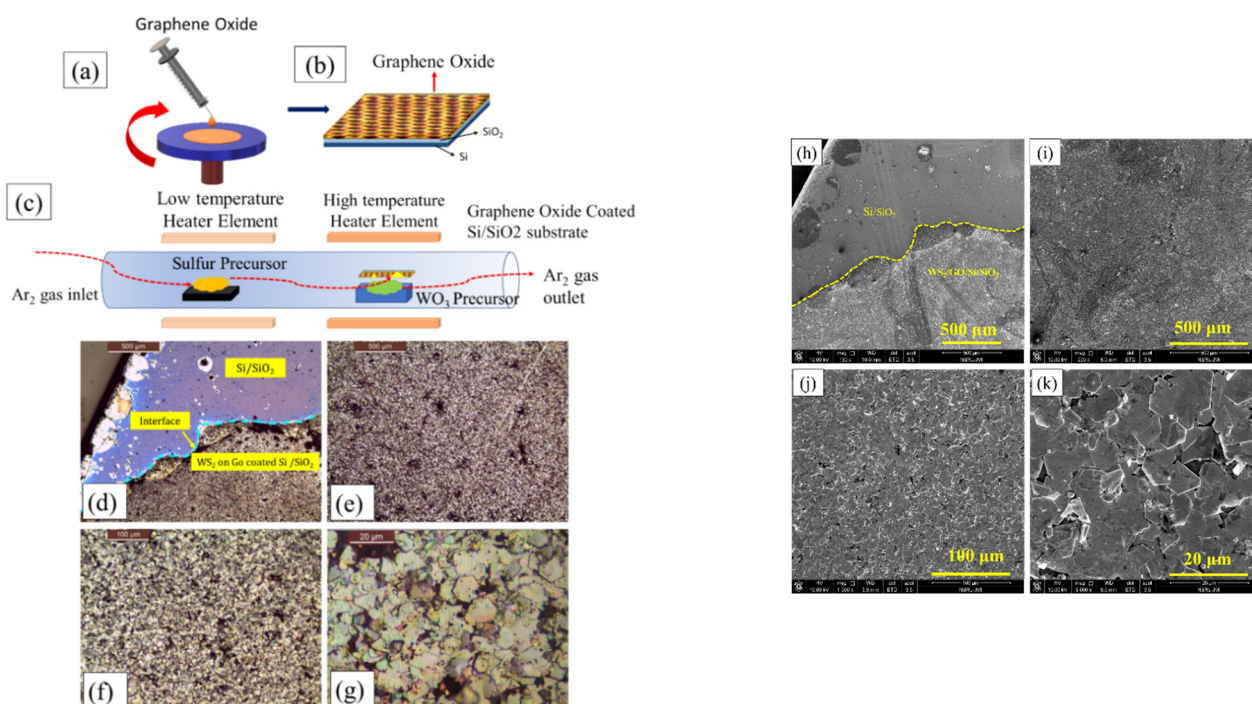

Figure 8. (**a**) Spin coating GO solution over Si/SiO$_2$ substrate, (**b**) GO coated Si/SiO$_2$ substrate, (**c**) CVD experimental setup used for WS$_2$ growth, and (**d**–**g**) optical microscope images of WS$_2$ grown on GO coated Si/SiO$_2$ substrate, and (**h**–**k**) FESEM micrographs of WS$_2$ grown over GO coated Si/SiO$_2$ substrate.
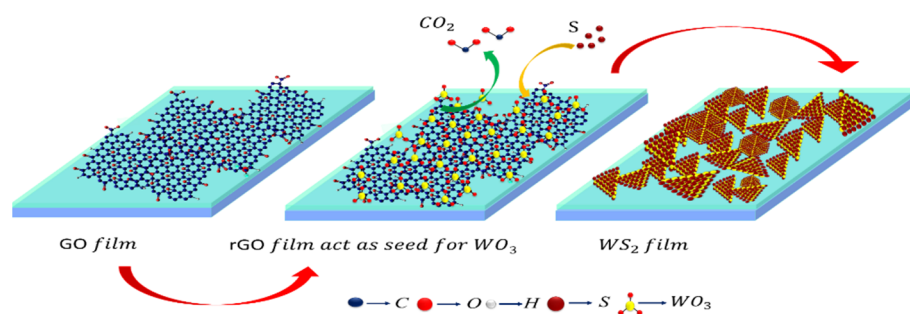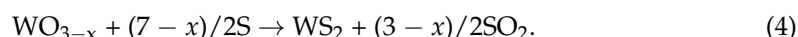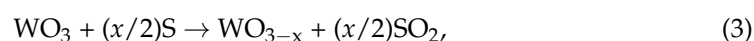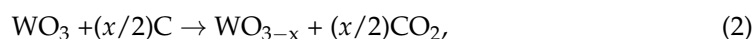
Figure 9. Schematic diagram to represent WS_2 growth mechanism on GO coated Si/SiO_2 substrate.

Upon heating, WO_3 vapors reach the surface of the substrate. A portion of these vapors diffuses and reacts with sp^2-bonded carbon patches of RGO, resulting in the formation of an intermediate phase, WO_{3-x}, along with the release of CO_2. Thus, an increase in the concentration of WO_3 vapors, results in simultaneous increase in the CO_2 and a corresponding decrease in the size of sp^2-carbon patches. Further, at elevated temperatures, WO_{3-x} molecules gain the tendency to migrate and aggregate around the sp^2-bonded carbon patches. These carbon patches or 'carbon nanostructures' are expected to act as heterogeneous nucleation sites; where nucleation takes place via sulfurization of adjoining WO_{3-x} molecules. The synthesis kinetics involve heterogeneous and homogeneous nucleation reactions, occurring simultaneously and competing with each other, as the main growth processes [61,62]. Initially, due to a lower surface free-energy barrier, heterogeneous nucleation outpaces the homogeneous nucleation [59]. In addition, the local high concentration of WO_{3-x} facilitates the formation of bilayer nuclei. In case of perfectly overlapping bilayer formation, the nucleation shifts from the bottom layer to the second layer almost instantly. If growth does not stop at this point, few-or multi-layer WS_2 flakes are formed. Nonetheless, a complete understanding of growth mechanics warrants further investigations. The growth process can be summarized in the following chemical reactions [61,62]:

$$WO_3 + (x/2)C \rightarrow WO_{3-x} + (x/2)CO_2, \tag{2}$$

$$WO_3 + (x/2)S \rightarrow WO_{3-x} + (x/2)SO_2, \tag{3}$$

$$WO_{3-x} + (7-x)/2S \rightarrow WS_2 + (3-x)/2SO_2. \tag{4}$$

The use of GO produces substantially different growth characteristics than the isolated islands observed during the first approach. The WS_2 islands now coalesce to form nearly continuous films on centimeter scale as is evident in the optical images and SEM micrograph (Figure 8). Apart from the monolayers, multilayered growth is also visible. The multilayered growth is more favored at either the nucleation sites or grain boundaries (the locations shown by pointing arrows). Continuous monoto-few layer growths on centimeter scale are representative of the samples grown via the second approach, where the Si/SiO_2 substrate is coated with GO. We have found the size of the individual WS_2 crystals less than 15 μm, which is much larger than those reported for h-BN substrates, where a domain size of less than 1 μm is observed [63–65]. Although it is smaller than the WS_2 grown on pristine Si/SiO_2 substrate, its continuous expansion on the entire substrate has strong merits and fulfils the objectives of this work, as well as the requisite need for device applications.

Figure 10a shows the Raman spectrum of a WS_2 film grown on GO coated substrate. The peaks present at 351.2 and 421.4 cm^{-1} is relatable with the E_{2g}^1 and A_{1g} Raman modes. Besides, the E_{2g}^1 and A_{1g} modes are found to be slightly red- and blue-shifted, respectively. Our concern is to study the shift in E_{2g}^1 and A_{1g} peaks due to thickness variation in a mixed multi-layered WS_2 flake. The increase in number of layers strongly enhances the out-of-plane vibrations, while coulomb interactions tend to decrease the frequency of in-plane vibrations, thereby causing monotonous increase in frequency separation between E_{2g}^1 and A_{1g} peaks [58]. While there is little variation in peak positions, small modifications in the

relative intensities between E_{2g}^{1} and A_{1g} modes are clearly observed. Samples synthesized via first approach have a slightly higher $E_{2g}{}^{1}$ intensity, with the ratio E_{2g}^{1}/A_{1g} of ~3.2. Conversely, the A_{1g} intensity is higher for the second approach, where E_{2g}^{1}/A_{1g} ratio is of ~1.25. Moderate changes in the Raman intensity ratio are believed to indicate changes in the number of layers for exfoliated WS_2 [46,66]. We have performed Raman mapping analysis at multiple spots of the same sample to confirm the uniformity of WS_2 across the substrate area as shown in Figure 10b,c. It is evident that there is slight variation in the separation as well as intensity ratio of in-plane and out-plane vibrational peaks as a function of sample spot location; and a summary of the peak position, difference in Raman peak frequency and intensity ratio of the peaks is tabulated in Table 1. The shift in the frequency of 2LA (M) and A_{1g} modes has been employed as a measure of the number of layers. However, this approach to determine the number of layers is erroneous due to the close proximity of 2LA (M) and E_{2g}^{1} phonon modes. It has been found that with increasing the number of layers, the intensity ratio $(I_{2LA(M)}/I_{A1g})$ decreases from 2.2 (for single layer) to 0.47 (for bulk) [64]. At the first instance, it looks the possible growth of mono- to few-layered WS_2. However, in case of monolayer MoS_2, such small intensity variations in $E_{2g}{}^{1}$ and A_{1g} peaks were correlated to the differences in electronic doping levels or strain as WS_2 and RGO effectively combine to form heterostructures [67]. Generally, TMDCs are highly prone to significant number of chalcogenide vacancies [59,64,65]. Sulphur vacancies exist in WS_2, thus introducing localized donor states deep inside the bandgap, which can be subsequently filled by environmental impurities to make it doped. As of now, various competitive approaches exist to find out the origin of anomaly in the interpretation of peak intensity ratio and shift in peak position of Raman modes. Nonetheless, the contribution to the intensity changes due to sulfur content in WS_2 films as a dopant, and local strain in between WS_2 and RGO, cannot be ignored [66].
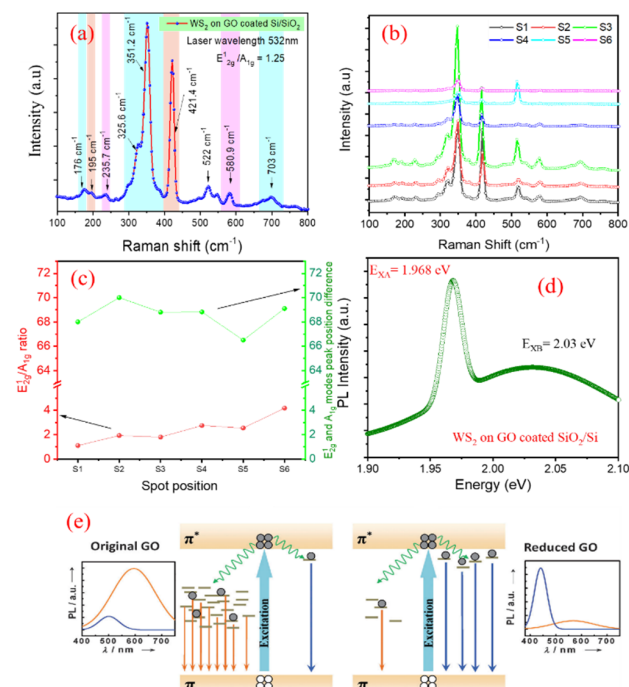

Figure 10. (**a**) Raman spectrum and (**b**) Raman spectra as a function of spot on different positions (**c**) Intensity ratio and difference of the peak as function of spot (**d**) Photoluminescence (PL) of WS_2 grown on GO coated Si/SiO_2 substrate, and (**e**) Evolution of PL spectra due to the transformation of sp^3- to sp^2-bonded region during the reduction of GO to RGO. Copyright Abid, Sehrawat, Islam, Mishra, Ahmad. Under a Creative Commons Attribution 4.0 International License. Reproduced with permission from [38]. Copyright 2012 Wiley

Table 1. Summary of Raman studies of WS$_2$ nanoflakes deposited on different spot of GO coated substrate.

Sample	Spot	Raman Peak Frequency (cm^{-1})		Frequency Difference	Intensity Ratio
		E_{2g}	A_{1g}		
WS$_2$/SiO$_2$/Si	1	354.3	421.1	66.7	1.75
	2	349.7	418.7	69	1.15
	3	350.1	419.2	69.1	0.96
	4	350.1	419.4	69.3	0.99
	5	352.4	419.3	66.9	1.2
	6	-	-	-	-
WS$_2$/GO/SiO$_2$/Si	S1	350.8	418.8	68.0	1.10
	S2	351.0	421.2	70.2	1.93
	S3	349.7	418.25	68.5	1.80
	S4	350.1	419.0	68.9	2.75
	S5	352.9	419.6	66.5	2.55
	S6	351.0	~420.1	69.1	4.19

The PL spectra, shown in Figure 10d, comprise with neutral A-exciton (X_A) at 1.968 eV as also observed in case of WS$_2$ growth on Si/SiO$_2$ substrate. A striking difference observed in WS$_2$ growth on GO-coated Si/SiO$_2$ substrate, is the appearance of a low intensity peak at 2.03 eV (611 nm), attributable to the weak transition of carriers from disorder induced states within π-π^* band structure of RGO [67] (schematically shown in Figure 10e). Our laser excitation visible wavelength does not cover the intense emission peak around 440 nm. A comparative study in terms of PL spectral positions, FWHM and shift in peak positions are put in Table 2. Surface roughness, in particular, the sharp edges, is reported to help in catalyst-free CNT growth [68]. To ascertain the role of surface roughness on the continuous growth of WS$_2$, we conducted CVD growth in identical conditions: first, on polished surface, marked with scratches on polished side of silicon wafer; and second, on backside, the unpolished surface of the same wafer. In the polished wafer side, WS$_2$ debris having no shape and sizes of flakes, are observed on and around the scratch marks. SEM images (Figure 11a–d) show few vertically aligned and flower petal shaped flakes with some horizontal flakes on the scratch marked region having negligible presence of triangular as well as hexagonal WS$_2$ crystallites.

Table 2. Summary of Photoluminescence (PL) studies of WS$_2$ nanoflakes deposited on different substrates.

Sample	Energy (eV)	FWHM (meV)	
	E_{XA}	E_{XA}	E_{XB}
WS$_2$/Si/SiO$_2$	1.968	25.3	-
WS$_2$/GO/SiO$_2$/Si	1.968	35.5	35.6

In contrast, we have achieved horizontally grown WS$_2$ crystallites, majority in hexagonal shape on the unpolished surface (Figure 11e–g). In both cases, thickness of WS$_2$ flake(s) is multilayered. It may be inferred that surface roughness does also play an important role in the WS$_2$ growth. The optical profilometer image (surface microscopy) of the GO coated sample surface before WS$_2$ deposition is shown in Figure 11h. It is to be noted that surface of RGO film is highly rough in nature; and this may be one of the sources of nucleation sites too, in addition to the major contribution from high density sp^2-bonded patches, to enhance the joining of grain boundaries, resulting in continuous WS$_2$ film growth over GO coated Si/SiO$_2$ substrate. Therefore, it may be understood that continuous growth

is possible in GO coated substrate, in which sp^2-patches of carbon purely act as a seed or catalyst that enhance growth origins.
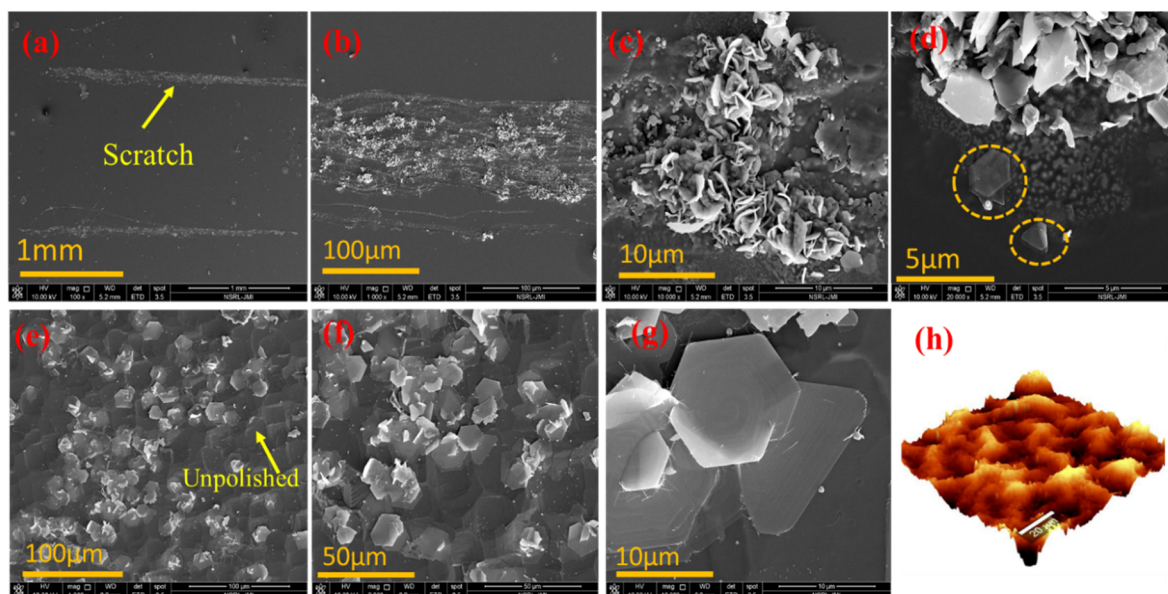

Figure 11. FESEM micrographs of WS_2 grown on scratch marks made on polished surface of Si wafer (**a–d**) and WS_2 grown on unpolished Si wafer (**e–g**). In both cases, other CVD growth parameters were constant. (**h**) The optical profilometer image (surface microscopy) of the GO coated sample surface before WS_2 deposition. The scale bar indicates the surface roughness of the sample close to 3.72 μm.

The present work has shown the successful growth of mono to few layer WS_2 film of square-centimeter size and triangular shape on graphene-oxide-coated Si/SiO$_2$ substrate using CVD technique. The real issue addressed in this work is the large area coverage of the WS_2 continuous film; however, many of the researchers have also tried to resolve this issue by using various approaches such as atomic layer deposition, pulse laser deposition, and metal/metal oxide thin film or noble metal substrates, etc. Although these strategies yield large area continuous TMDCs, these techniques also suffer from high costs, increased complexity, and sometimes poor quality. Further, to be useful, WS_2 grown over inert metal needs etching via acidic or basic (e.g., concentrated HF, KOH and NaOH) solutions, before transferring to Si or flexible substrates. Usually, the transfer processes not only end up in damaging the grown material (WS_2), but produce substrate residues and negative environment impact, as well. We successfully grew the continuous WS_2 film at very low cost by simply coating the Si/SiO$_2$ substrate with graphene oxide (GO) and this technique is highly reproducible. Table 3 enlists the optical properties of WS_2 nanoflakes deposited on different substrates. However, HRTEM and Raman spectroscopy confirm the high crystallinity and quality of the grown WS_2 flakes. Note that the Raman peak frequencies difference (66–72 cm^{-1}) and the PL peak position (2.00–1.92 eV) as well as intensity fluctuates over the WS_2 triangles as enlisted in Table 2. The change of frequency and/or width of Raman modes of 2H-type transition-metal dichalcogenides can be used to evaluate the sample quality because they are strongly sensitive to external electrostatic doping (A_{1g} mode) and lattice strain (E_{2g}^1 mode) [69,70]. Wang et al. found that E_{2g}^1 mode exhibits obvious red-shift when increasing strain [70]. In contrast, Chakraborty demonstrated that a softening and broadening of the A_{1g} mode occur with electron doping, whereas the E_{2g}^1 mode remains essentially inert [69].

Table 3. Summary of optical properties of WS$_2$ nanoflakes deposited on different substrates.

Sample	Raman Peak Frequency (cm^{-1})		A-Exciton Energy (eV)	Ref.
	E_{2g}	A_{1g}		
WS$_2$/Al$_2$O$_3$	352.7	421.2	2.000	[10]
WS$_2$/SiO$_2$/Si	353.0	418.3	1.920	[18]
WS$_2$/Au	356.2	420.9	1.935	[25]
WS$_2$/SiO$_2$/Si	352.5	419.0	1.977	[12]
WS$_2$/sapphire	354.0	412.0	2.000	[26]
WS$_2$/SiO$_2$/Si	~350	~416	1.949	[28]
WS$_2$/SiO$_2$/Si	354.0	421.0	1.968	this work
WS$_2$/GO/SiO$_2$/Si	351.2	421.4	1.968	this work

- Photoconductive response of sensor prepared with GO coated Si/SiO$_2$

To check the continuity of the grown film, I-V characteristics were monitored in the voltage range of −12 V to +12 V using Keithley SCS 4200 for variable channel length (from 0.5 to 5.0 mm). The inset of Figure 12a shows the digital photographs of the samples, where the electrical probes are set at different channel lengths. The observed I-V curves indicate that flakes grown over the GO modified substrate are interconnecting and form a continuous network. Figure 12b demonstrates the possible use of developed film as photodetector where the change in photocurrent under illumination of laser wavelength of 635 nm, keeping the laser power constant at 40 mW, is shown. The cyclic response is highly reproducible with negligible drift. The photoresponsivity and specific detectivity are found to be 0.9 µA W^{-1} and 0.15 × 10^5 jones.
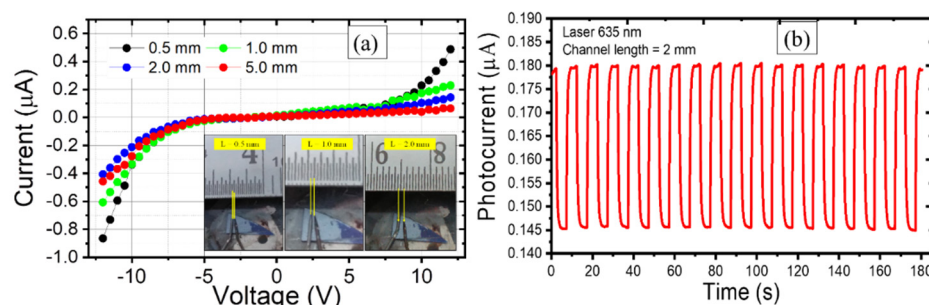
Figure 12. (**a**) Current vs. voltage characteristics at variable channel length and (**b**) photoconductive response under laser wavelength 635 nm.

4. Conclusions

Efforts have been made to understand the growth mechanics of large domain size of mono-to-few layer growth of WS$_2$. Nature of substrate is utilized to understand the intricate mechanism behind continuous film growth. Large area (domain size of around 60 µm), mono-to-few layer WS$_2$ crystals of triangular shape, were grown on pristine Si/SiO$_2$ and GO-coated Si/SiO$_2$ substrates, using CVD technique with a two-zone furnace. For GO coated Si/SiO$_2$ substrate, uniform mono-to-few layer growth of WS$_2$ crystals is achieved, although the size of WS$_2$ crystals is smaller than those grown on pristine Si/SiO$_2$ substrate. In case of growth on Si/SiO$_2$ substrate, monolayer WS$_2$ grain boundaries are in isolation, and highly scattered on the substrate surface. Further tests were conducted to examine the role of surface roughness, as reported in the past for catalyst-free CNT growth on pristine silicon surface. We conducted CVD growth in identical conditions, one on polished surface, marked with scratches; and the other one, on the unpolished surface of the same wafer. Strikingly, WS$_2$ growth exclusively on rough surface in both the cases, confirmed that surface roughness does play an important role. In addition, high density

sp^2-bonded patches enhance the joining of grain boundaries, to enable continuous WS_2 film growth over GO coated Si/SiO_2 substrate. It is concluded that the combination of high-temperature CVD with reduced graphene oxide surface is supposed to be a favorable condition for TMDCs growth with full coverage of the substrate. The idea of GO coated Si/SiO_2 substrate may be employed for mass production of identical devices, and therefore bids for commercial scale development and can be extended to other TMDCs.

Appendix A

Photoresponsivity (R_λ)

The ratio of photocurrent to the incident intensity of the laser wavelength λ is defined as photoresponsivity of the photodetector and it can be calculated as [71]:

$$R_\lambda = \frac{\Delta I_{ph}}{P \cdot A}. \tag{A1}$$

Photosensitivity (S)

It is defined as the ratio of change in current under illumination and dark current [72]:

$$S\ (\%) = \frac{I_{photo} - I_{Dark}}{I_{Dark}} \times 100. \tag{A2}$$

Specific Detectivity

It represents the ability of the detector to capture the weakest signal, which can be mathematically expressed as [71]:

$$D = \frac{R_\lambda \sqrt{A}}{\sqrt{2eI_{Dark}}}, \tag{A3}$$

where A represents the effective area of photodetector, and e is the electronic charge.

References

1. Cong, C.; Shang, J.; Wang, Y.; Yu, T. Optical properties of 2D semiconductor WS_2. *Adv. Opt. Mater.* **2018**, *6*, 1700767. [CrossRef]
2. Park, J.; Kim, M.S.; Cha, E.; Kim, J.; Choi, W. Synthesis of uniform single layer WS_2 for tunable photoluminescence. *Sci. Rep.* **2017**, *7*, 1–8. [CrossRef] [PubMed]
3. Rafiq, M.K.S.B.; Amin, N.; Alharbi, H.F.; Luqman, M.; Ayob, A.; Alharthi, Y.S.; Alharthi, N.H.; Bais, B.; Akhtaruzzaman, M. WS_2: A New Window Layer Material for Solar Cell Application. *Sci. Rep.* **2020**, *10*, 1–11.
4. Gutiérrez, H.R.; Perea-López, N.; Elías, A.L.; Berkdemir, A.; Wang, B.; Lv, R.; López-Urías, F.; Crespi, V.H.; Terrones, H.; Terrones, M. Extraordinary room-temperature photoluminescence in triangular WS_2 monolayers. *Nano Lett.* **2013**, *13*, 3447–3454. [CrossRef] [PubMed]

5. Tanoh, A.O.A.; Alexander-Webber, J.; Xiao, J.; Delport, G.; Williams, C.A.; Bretscher, H.; Gauriot, N.; Allardice, J.; Pandya, R.; Fan, Y.; et al. Enhancing photoluminescence and mobilities in WS$_2$ monolayers with oleic acid ligands. *Nano Lett.* **2019**, *19*, 6299–6307. [CrossRef] [PubMed]

6. Yuan, L.; Huang, L. Exciton dynamics and annihilation in WS$_2$ 2D semiconductors. *Nanoscale* **2015**, *7*, 7402–7408. [CrossRef]

7. Zhu, B.; Chen, X.; Cui, X. Exciton binding energy of monolayer WS$_2$. *Sci. Rep.* **2015**, *5*, 9218. [CrossRef]

8. Ye, Z.; Cao, T.; O'brien, K.; Zhu, H.; Yin, X.; Wang, Y.; Louie, S.G.; Zhang, X. Probing excitonic dark states in single-layer tungsten disulphide. *Nature* **2014**, *513*, 214–218. [CrossRef]

9. Peimyoo, N.; Shang, J.; Cong, C.; Shen, X.; Wu, X.; Yeow, E.K.; Yu, T. Nonblinking, intense two-dimensional light emitter: Monolayer WS$_2$ triangles. *ACS Nano* **2013**, *7*, 10985–10994. [CrossRef]

10. Lan, F.; Yang, R.; Xu, Y.; Qian, S.; Zhang, S.; Cheng, H.; Zhang, Y. Synthesis of large-scale single-crystalline monolayer WS$_2$ using a semi-sealed Method. *Nanomaterials* **2018**, *8*, 100. [CrossRef]

11. Zhang, Q.; Lu, J.; Wang, Z.; Dai, Z.; Zhang, Y.; Huang, F.; Bao, Q.; Duan, W.; Fuhrer, M.S.; Zheng, C. Reliable synthesis of large-area monolayer WS$_2$ single crystals, films, and heterostructures with extraordinary photoluminescence induced by water intercalation. *Adv. Opt. Mater.* **2018**, *6*, 1701347. [CrossRef]

12. Liu, P.; Luo, T.; Xing, J.; Xu, H.; Hao, H.; Liu, H.; Dong, J. Large-area WS$_2$ film with big single domains grown by chemical vapor deposition. *Nanoscale Res. Lett.* **2017**, *12*, 558. [CrossRef] [PubMed]

13. Wang, Q.H.; Kalantar-Zadeh, K.; Kis, A.; Coleman, J.N.; Strano, M.S. Electronics and optoelectronics of two-dimensional transition metal dichalcogenides. *Nat. Nanotechnol.* **2012**, *7*, 699. [CrossRef] [PubMed]

14. Dong, R.; Kuljanishvili, I. Progress in fabrication of transition metal dichalcogenides heterostructure systems. *J. Vac. Sci. Technol. B* **2017**, *35*, 030803. [CrossRef] [PubMed]

15. Yuan, L.; Ge, J.; Peng, X.; Zhang, Q.; Wu, Z.; Jian, Y.; Xiong, X.; Yin, H.; Han, J. A reliable way of mechanical exfoliation of large scale two dimensional materials with high quality. *AIP Adv.* **2016**, *6*, 125201. [CrossRef]

16. Ghorai, A.; Midya, A.; Maiti, R.; Ray, S.K. Exfoliation of WS$_2$ in the semiconducting phase using a group of lithium halides: A new method of Li intercalation. *Dalton Trans.* **2016**, *45*, 14979–14987. [CrossRef]

17. Nicolosi, V.; Chhowalla, M.; Kanatzidis, M.G.; Strano, M.S.; Coleman, J.N. Liquid exfoliation of layered materials. *Science* **2013**, *340*, 1226419. [CrossRef]

18. Elías, A.L.; Perea-López, N.; Castro-Beltrán, A.; Berkdemir, A.; Lv, R.; Feng, S.; Long, A.D.; Hayashi, T.; Kim, Y.A.; Endo, M.; et al. Controlled synthesis and transfer of large-area WS$_2$ sheets: From single layer to few layers. *ACS Nano* **2013**, *7*, 5235–5242. [CrossRef]

19. Cao, S.; Liu, T.; Hussain, S.; Zeng, W.; Peng, X.; Pan, F. Hydrothermal synthesis of variety low dimensional WS$_2$ nanostructures. *Mater. Lett.* **2014**, *129*, 205–208. [CrossRef]

20. Alonso, G.; Petranovskii, V.; Del Valle, M.; Cruz-Reyes, J.; Licea-Claverie, A.; Fuentes, S. Preparation of WS2 catalysts by in situ decomposition of tetraalkylammonium thiotungstates. *Appl. Catal. A* **2000**, *197*, 87–97. [CrossRef]

21. Balasubramanyam, S.; Shirazi, M.; Bloodgood, M.A.; Wu, L.; Verheijen, M.A.; Vandalon, V.; Kessels, W.M.; Hofmann, J.P.; Bol, A.A. Edge-site nanoengineering of WS$_2$ by low-temperature plasma-enhanced atomic layer deposition for electrocatalytic hydrogen evolution. *Chem. Mater.* **2019**, *31*, 5104–5115. [CrossRef] [PubMed]

22. Loh, T.A.; Chua, D.H.; Wee, A.T. One-step synthesis of few-layer WS$_2$ by pulsed laser deposition. *Sci. Rep.* **2015**, *5*, 18116. [CrossRef] [PubMed]

23. Tian, K.; Baskaran, K.; Tiwari, A. Growth of two-dimensional WS$_2$ thin films by pulsed laser deposition technique. *Thin Solid Film.* **2018**, *668*, 69–73. [CrossRef]

24. Koçak, Y.; Akaltun, Y.; Gür, E. Magnetron sputtered WS$_2$; optical and structural analysis. *J. Phys. Conf. Ser.* **2016**, *707*, 012028. [CrossRef]

25. Gao, Y.; Liu, Z.; Sun, D.M.; Huang, L.; Ma, L.P.; Yin, L.C.; Ma, T.; Zhang, Z.; Ma, X.L.; Peng, L.M.; et al. Large-area synthesis of high-quality and uniform monolayer WS$_2$ on reusable Au foils. *Nat. Commun.* **2015**, *6*, 8569. [CrossRef] [PubMed]

26. Xu, Z.Q.; Zhang, Y.; Lin, S.; Zheng, C.; Zhong, Y.L.; Xia, X.; Li, Z.; Sophia, P.J.; Fuhrer, M.S.; Cheng, Y.B.; et al. Synthesis and transfer of large-area monolayer WS$_2$ crystals: Moving toward the recyclable use of sapphire substrates. *ACS Nano* **2015**, *9*, 6178–6187. [CrossRef]

27. Yu, J.; Li, J.; Zhang, W.; Chang, H. Synthesis of high quality two-dimensional materials via chemical vapor deposition. *Chem. Sci.* **2015**, *6*, 6705–6716. [CrossRef]

28. Rong, Y.; Fan, Y.; Koh, A.L.; Robertson, A.W.; He, K.; Wang, S.; Tan, H.; Sinclair, R.; Warner, J.H. Controlling sulphur precursor addition for large single crystal domains of WS$_2$. *Nanoscale* **2014**, *6*, 12096–12103. [CrossRef]

29. Okada, M.; Okada, N.; Chang, W.H.; Endo, T.; Ando, A.; Shimizu, T.; Kubo, T.; Miyata, Y.; Irisawa, T. Gas-source CVD growth of atomic layered WS$_2$ from WF$_6$ and H$_2$S precursors with high grain size uniformity. *Sci. Rep.* **2019**, *9*, 1–10. [CrossRef]

30. Lu, Y.; Chen, T.; Ryu, G.H.; Huang, H.; Sheng, Y.; Chang, R.J.; Warner, J.H. Self-limiting growth of high-quality 2D monolayer MoS$_2$ by direct sulfurization using precursor-soluble substrates for advanced field-effect transistors and photodetectors. *ACS Appl. Nano Mater.* **2018**, *2*, 369–378. [CrossRef]

31. Kim, Y.; Song, J.G.; Park, Y.J.; Ryu, G.H.; Lee, S.J.; Kim, J.S.; Jeon, P.J.; Lee, C.W.; Woo, W.J.; Choi, T.; et al. Self-limiting layer synthesis of transition metal dichalcogenides. *Sci. Rep.* **2016**, *6*, 18754. [CrossRef] [PubMed]

32. Zhang, Y.; Zhang, Y.; Ji, Q.; Ju, J.; Yuan, H.; Shi, J.; Gao, T.; Ma, D.; Liu, M.; Chen, Y.; et al. Controlled growth of high-quality monolayer WS2 layers on sapphire and imaging its grain boundary. *ACS Nano* **2013**, *7*, 8963–8971. [CrossRef] [PubMed]

33. Cong, C.; Shang, J.; Wu, X.; Cao, B.; Peimyoo, N.; Qiu, C.; Sun, L.; Yu, T. Synthesis and optical properties of large-area single-crystalline 2D semiconductor WS$_2$ monolayer from chemical vapor deposition. *Adv. Opt. Mater.* **2014**, *2*, 131–136. [CrossRef]

34. Li, S.; Wang, S.; Tang, D.M.; Zhao, W.; Xu, H.; Chu, L.; Bando, Y.; Golberg, D.; Eda, G. Halide-assisted atmospheric pressure growth of large WSe$_2$ and WS$_2$ monolayer crystals. *Appl. Mater. Today* **2015**, *1*, 60–66. [CrossRef]

35. Kang, K.N.; Godin, K.; Yang, E.H. The growth scale and kinetics of WS$_2$ monolayers under varying H$_2$ concentration. *Sci. Rep.* **2015**, *5*, 1–9. [CrossRef] [PubMed]

36. Liu, Z.; Murphy, A.W.A.; Kuppe, C.; Hooper, D.C.; Valev, V.K.; Ilie, A. WS$_2$ Nanotubes, 2D nanomeshes, and 2D in-plane films through one single chemical vapor deposition route. *ACS Nano* **2019**, *13*, 3896–3909. [CrossRef] [PubMed]

37. Lee, Y.H.; Zhang, X.Q.; Zhang, W.; Chang, M.T.; Lin, C.T.; Chang, K.D.; Yu, Y.C.; Wang, J.T.W.; Chang, C.S.; Li, L.J.; et al. Synthesis of large-area MoS$_2$ atomic layers with chemical vapor deposition. *Adv. Mater.* **2012**, *24*, 2320–2325. [CrossRef]

38. Abid; Sehrawat, P.; Islam, S.S.; Mishra, P.; Ahmad, S. Reduced graphene oxide (rGO) based wideband optical sensor and the role of temperature, defect states and quantum efficiency. *Sci. Rep.* **2018**, *8*, 1–13. [CrossRef]

39. Sehrawat, P.; Islam, S.S.; Mishra, P. Reduced graphene oxide based temperature sensor: Extraordinary performance governed by lattice dynamics assisted carrier transport. *Sens. Actuators B* **2018**, *258*, 424–435. [CrossRef]

40. Sehrawat, P.; Islam, S.S. An ultrafast quantum thermometer from graphene quantum dots. *Nanoscale Adv.* **2019**, *1*, 1772–1783. [CrossRef]

41. Zhang, X.; Nan, H.; Xiao, S.; Wan, X.; Gu, X.; Du, A.; Ni, Z.; Ostrikov, K.K. Transition metal dichalcogenides bilayer single crystals by reverse-flow chemical vapor epitaxy. *Nat. Commun.* **2019**, *10*, 1–10. [CrossRef] [PubMed]

42. Yan, J.; Xia, J.; Wang, X.; Liu, L.; Kuo, J.L.; Tay, B.K.; Chen, S.; Zhou, W.; Liu, Z.; Shen, Z.X. Stacking-dependent interlayer coupling in trilayer MoS$_2$ with broken inversion symmetry. *Nano Lett.* **2015**, *15*, 8155–8161. [CrossRef] [PubMed]

43. Jeong, H.Y.; Jin, Y.; Yun, S.J.; Zhao, J.; Baik, J.; Keum, D.H.; Lee, H.S.; Lee, Y.H. Heterogeneous defect domains in single-crystalline hexagonal WS$_2$. *Adv. Mater.* **2017**, *29*, 1605043. [CrossRef] [PubMed]

44. Yue, Y.; Chen, J.; Zhang, Y.; Ding, S.; Zhao, F.; Wang, Y.; Zhang, D.; Li, R.; Dong, H.; Hu, W.; et al. Two-dimensional high-quality monolayered triangular WS$_2$ flakes for field-effect transistors. *ACS Appl. Mater. Interfaces* **2018**, *10*, 22435–22444. [CrossRef] [PubMed]

45. Chen, F.; Ding, S.; Su, W. A feasible approach to fabricate two-dimensional WS$_2$ flakes: From monolayer to multilayer. *Ceram. Int.* **2018**, *44*, 22108–22112. [CrossRef]

46. McCreary, K.M.; Hanbicki, A.T.; Jernigan, G.G.; Culbertson, J.C.; Jonker, B.T. Synthesis of large-area WS$_2$ monolayers with exceptional photoluminescence. *Sci. Rep.* **2016**, *6*, 19159. [CrossRef]

47. Boson, A.J. Chemical Vapor Deposition of Two-Dimensional Materials and Heterostructures. Ph.D. Thesis, University of Nebraska-Lincoln, Lincoln, NE, USA, 2017. Available online: https://digitalcommons.unl.edu/cgi/viewcontent.cgi?article=1083&context=chemistrydiss (accessed on 28 April 2017).

48. Xiao, J.; Zhao, M.; Wang, Y.; Zhang, X. Excitons in atomically thin 2D semiconductors and their applications. *Nanophotonics* **2017**, *6*, 1309–1328. [CrossRef]

49. Mitioglu, A.A.; Plochocka, P.; Jadczak, J.N.; Escoffier, W.; Rikken, G.L.J.A.; Kulyuk, L.; Maude, D.K. Optical manipulation of the exciton charge state in single-layer tungsten disulfide. *Phys. Rev. B* **2013**, *88*, 245403. [CrossRef]

50. Paur, M.; Molina-Mendoza, A.J.; Bratschitsch, R.; Watanabe, K.; Taniguchi, T.; Mueller, T. Electroluminescence from multi-particle exciton complexes in transition metal dichalcogenide semiconductors. *Nat. Commun.* **2019**, *10*, 1–7. [CrossRef]

51. Chernikov, A.; Berkelbach, T.C.; Hill, H.M.; Rigosi, A.; Li, Y.; Aslan, O.B.; Reichman, D.R.; Hybertsen, M.S.; Heinz, T.F. Exciton binding energy and nonhydrogenic Rydberg series in monolayer WS$_2$. *Phys. Rev. Lett.* **2014**, *113*, 076802. [CrossRef]

52. Shang, J.; Shen, X.; Cong, C.; Peimyoo, N.; Cao, B.; Eginligil, M.; Yu, T. Observation of excitonic fine structure in a 2D transition-metal dichalcogenide semiconductor. *ACS Nano* **2015**, *9*, 647–655. [CrossRef] [PubMed]

53. Ren, D.D.; Qin, J.K.; Li, Y.; Miao, P.; Sun, Z.Y.; Xu, P.; Zhen, L.; Xu, C.Y. Photoluminescence inhomogeneity and excitons in CVD-grown monolayer WS$_2$. *Opt. Mater.* **2018**, *80*, 203–208. [CrossRef]

54. Carozo, V.; Wang, Y.; Fujisawa, K.; Carvalho, B.R.; McCreary, A.; Feng, S.; Lin, Z.; Zhou, C.; Perea-López, N.; Elías, A.L.; et al. Optical identification of sulfur vacancies: Bound excitons at the edges of monolayer tungsten disulfide. *Sci. Adv.* **2017**, *3*, e1602813. [CrossRef] [PubMed]

55. Zhao, W.; Ghorannevis, Z.; Chu, L.; Toh, M.; Kloc, C.; Tan, P.H.; Eda, G. Evolution of electronic structure in atomically thin sheets of WS$_2$ and WSe$_2$. *ACS Nano* **2013**, *7*, 791–797. [CrossRef] [PubMed]

56. Mak, K.F.; He, K.; Lee, C.; Lee, G.H.; Hone, J.; Heinz, T.F.; Shan, J. Tightly bound trions in monolayer MoS$_2$. *Nat. Mater.* **2013**, *12*, 207–211. [CrossRef]

57. Ross, J.S.; Wu, S.; Yu, H.; Ghimire, N.J.; Jones, A.M.; Aivazian, G.; Yan, J.; Mandrus, D.G.; Xiao, D.; Yao, W.; et al. Electrical control of neutral and charged excitons in a monolayer semiconductor. *Nat. Commun.* **2013**, *4*, 1–6. [CrossRef]

58. Zeng, H.; Liu, G.B.; Dai, J.; Yan, Y.; Zhu, B.; He, R.; Xie, L.; Xu, S.; Chen, X.; Yao, W.; et al. Optical signature of symmetry variations and spin-valley coupling in atomically thin tungsten dichalcogenides. *Sci. Rep.* **2013**, *3*, 1608. [CrossRef]

59. McCreary, A.; Berkdemir, A.; Wang, J.; Nguyen, M.A.; Elías, A.L.; Perea-López, N.; Fujisawa, K.; Kabius, B.; Carozo, V.; Cullen, D.A.; et al. Distinct photoluminescence and Raman spectroscopy signatures for identifying highly crystalline WS 2 monolayers produced by different growth methods. *J. Mater. Res.* **2016**, *31*, 931–944. [CrossRef]

60. McCreary, K.M.; Hanbicki, A.T.; Singh, S.; Kawakami, R.K.; Jernigan, G.G.; Ishigami, M.; Ng, A.; Brintlinger, T.H.; Stroud, R.M.; Jonker, B.T. The effect of preparation conditions on Raman and photoluminescence of monolayer WS_2. *Sci. Rep.* **2016**, *6*, 35154. [CrossRef]

61. Liang, J.; Zhang, L.; Li, X.; Pan, B.; Luo, T.; Liu, D.; Zou, C.; Liu, N.; Hu, Y.; Yang, K.; et al. Carbon-nanoparticle-assisted growth of high quality bilayer WS_2 by atmospheric pressure chemical vapor deposition. *Nano Res.* **2019**, *12*, 2802–2807. [CrossRef]

62. Okada, M.; Sawazaki, T.; Watanabe, K.; Taniguch, T.; Hibino, H.; Shinohara, H.; Kitaura, R. Direct chemical vapor deposition growth of WS_2 atomic layers on hexagonal boron nitride. *ACS Nano* **2014**, *8*, 8273–8277. [CrossRef] [PubMed]

63. Molas, M.R.; Nogajewski, K.; Potemski, M.; Babiński, A. Raman scattering excitation spectroscopy of monolayer WS_2. *Sci. Rep.* **2017**, *7*, 1–8. [CrossRef] [PubMed]

64. Botello Méndez, A.R.; Perea López, N.; Elías Arriaga, A.L.; Crespi, V.; López Urías, F.; Terrones Maldonado, H.; Terrones Maldonado, M. Identification of individual and few layers of WS_2 using Raman spectroscopy. *Sci. Rep.* **2013**, *3*, 1755.

65. Gołasa, K.; Grzeszczyk, M.; Bożek, R.; Leszczyński, P.; Wysmołek, A.; Potemski, M.; Babiński, A. Resonant Raman scattering in MoS_2—From bulk to monolayer. *Solid State Commun.* **2014**, *197*, 53–56. [CrossRef]

66. Buscema, M.; Steele, G.A.; van der Zant, H.S.; Castellanos-Gomez, A. The effect of the substrate on the Raman and photoluminescence emission of single-layer MoS_2. *Nano Res.* **2014**, *7*, 561–571. [CrossRef]

67. Chien, C.T.; Li, S.S.; Lai, W.J.; Yeh, Y.C.; Chen, H.A.; Chen, I.S.; Chen, L.C.; Chen, K.H.; Nemoto, T.; Isoda, S.; et al. Tunable photoluminescence from graphene oxide. *Angew. Chem. Int. Ed.* **2012**, *51*, 6662–6666. [CrossRef]

68. Tripathi, N.; Mishra, P.; Joshi, B.; Islam, S.S. Catalyst free, excellent quality and narrow diameter of CNT growth on Al_2O_3 by a thermal CVD technique. *Phys. E* **2014**, *62*, 43–47. [CrossRef]

69. Chakraborty, B.; Matte, H.R.; Sood, A.K.; Rao, C.N.R. Layer-dependent resonant Raman scattering of a few layer MoS_2. *J. Raman Spectr.* **2013**, *44*, 92–96. [CrossRef]

70. Wang, Y.; Cong, C.; Qiu, C.; Yu, T. Raman spectroscopy study of lattice vibration and crystallographic orientation of monolayer MoS_2 under uniaxial strain. *Small* **2013**, *9*, 2857–2861. [CrossRef]

71. Talib, M.; Tabassum, R.; Islam, S.S.; Mishra, P. Improvements in the performance of a visible–NIR photodetector using horizontally aligned TiS_3 nanoribbons. *ACS Omega* **2019**, *4*, 6180–6191. [CrossRef]

72. Abid; Sehrawat, P.; Islam, S.S.; Gulati, P.; Talib, M.; Mishra, P.; Khanuja, M. Development of highly sensitive optical sensor from carbon nanotube-alumina nanocomposite free-standing films: CNTs loading dependence sensor performance analysis. *Sens. Actuators A* **2018**, *269*, 62–69. [CrossRef]